Hetero-confinement in single CdTe nanoplatelets

Tasnim Ahmed,[#] Xuanheng Tan,[#] Barry Y. Li, Jillian Williams, Elijah Cook, Sophia M. Tiano[†], Stephanie M. Tenney, Dugan Hayes[†], Justin R. Caram*

Department of Chemistry and Biochemistry, University of California, Los Angeles, 607 Charles E. Young Drive, Los Angeles, California 90095-1569, United States

[†]Department of Chemistry, University of Rhode Island, Kingston, Rhode Island 02881, United States

Abstract:

Dimension-engineered synthesis of atomically thin II-VI nanoplatelets (NPLs) remains an open challenge. While CdSe NPLs have been made with confinement ranging from 2-11 monolayers (ML), CdTe NPLs have been significantly more challenging to synthesize and separate. Here we provide detailed mechanistic insight into the layer-by-layer growth kinetics of CdTe NPLs. Combining ensemble and single particle spectroscopic and microscopic tools, our work suggests that beyond 2 ML CdTe NPLs, higher ML structures initially appear as hetero-confined materials with co-localized multilayer structures. In particular, we observe strongly colocalized 3 and 4 ML emissions accompanied by a broad trap emission. Accompanying transient absorption, single particle optical and atomic force microscopy suggests islands of different MLs on the same NPL. To explain the non-standard nucleation and growth of these hetero-confined structures, we simulated the growth conditions of NPLs and quantified how monomer binding energy modifies the kinetics and permits single NPLs with multi-ML structures. Our findings suggest that the lower bond energy associated with CdTe relative to CdSe limits higher ML syntheses and explains the observed differences between CdTe and CdSe growth.

TOC

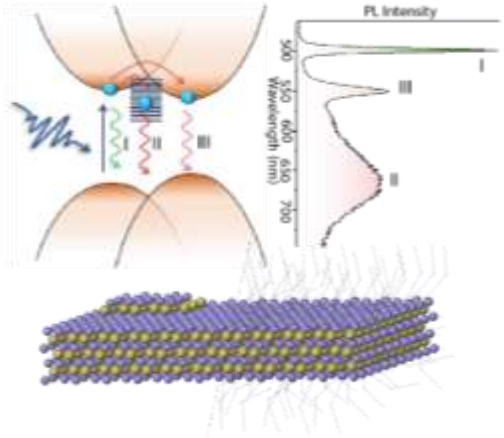

Introduction:

In recent years significant effort has gone into controlling the size, composition, and dimensionality of semiconducting nanocrystals.[1–3] By changing the latter, chemists have synthesized tunable quantum dots, rods, and nanoplatelet (NPL) structures (0-, 1- and 2-D materials respectively). NPLs in particular show control over the band gap with the change of thickness dimension.[4,5] Furthermore, while the lateral dimensions of these NPLs can range from tens of nanometers to micrometers, the optical properties are mainly controlled by the thickness dimension allowing for nearly homogeneous absorption and emission properties.[6] The 1D confinement in these systems results in unique optical and electronic properties including spectrally pure photoluminescence (PL), large absorption cross-sections, boosted optical gain, high-efficiency energy transfer, and surface dielectric/strain tunable exciton binding energies.[3,4,7–10] Although the unique behaviors make them a promising material for applications in lasers, field-

effect transistors, solar cells, and light-emitting devices,[9,11–15] the basic understanding of the mechanism behind the anisotropic growth of those NPLs is still hotly debated.[8,16,17]

Among the various Cd-chalcogenide systems, CdSe NPLs have been the most investigated with researchers exercising control over thicknesses (N ML zinc-blende NPLs consist of N layers of Te/Se/S and N+1 layers of Cd) and hetero-structure type (e.g., alloy, core-shell and core-crown) and incorporating them into applications (from lasing to scintillation).[18–23] In contrast, despite the reported synthesis of CdTe quantum dots and nanorods,[24–31] NPLs of this composition remain relatively understudied regardless of intriguing properties including a lower band gap for bulk CdTe (1.44eV compared to 1.74eV/2.24eV for CdSe/CdS)[32], larger area NPL structures, and potential connections to the large market for photovoltaic and photodetection devices.[27,33]

Being of the same II-VI semiconductor family, CdTe and CdSe NPLs show well-separated and sharp absorbance of heavy-hole and light-hole excitonic transitions, giant oscillator strength transitions, and narrow and tunable emission, but there are a few clear differences in their chemistry and photophysical properties.[32] While distinct and easily separable thickness populations are demonstrated for CdSe, a mixture of different thicknesses of NPLs is often observed in CdTe NPLs along with broad trap emission, which were first reported by Ithurria *et al*.[34] CdSe NPLs have been directly synthesized of thickness 2 ML to 5 ML, while Pedetti *et al*. demonstrated how factors such as reaction temperature, ligand concentration, synthetic precursors, and injection rate can be manipulated to achieve three different thickness (2 ML to 4 ML) of CdTe NPLs populations with reduced contribution from other thicknesses.[35] However, a contribution from broad trap emission is also observed for 3 and 4 ML NPLs.[35] Chu *et al*. were able to synthesize 11 ML CdSe but also without clear separation of thickness[36]. Using the dissolution/recrystallization method, Moghaddam et at. were able to increase the thickness of CdSe

NPLs up to 9 ML starting from 3 ML for CdSe NPLs; CdTe thickness reached 5 ML starting from 3ML as reflected in the absorption spectra, but again clear separation was not observed for thick NPLs.[22] Furthermore, synthesized CdTe NPLs also display a significantly lower photoluminescence quantum yield (PLQY) when compared to their CdSe cousins.[30–34] In the case of CdSe NPLs without any shell, PLQY can reach up to 40-50%[21] whereas CdTe NPL PLQY is typically less than 1%.[35] Recent work by Anand *et al*.[37] demonstrated improved PLQY of 9% in small-area 3 ML CdTe NPLs by quenching the reaction with cadmium propionate (a Z-type ligand) instead of oleic acid. Similarly, Al-Shnani *et al*.[38] showed PLQY up to 12% by using a different Te source and post-synthetic treatment. However, despite these improvements, contributions from other ML NPLs and trap emissions were observed for thick CdTe NPLs.[34,35,37,38]

In this work, we studied the growth of CdTe NPLs during their formation following fast injection and focused on the factors that make it challenging to synthesize high-purity CdTe NPLs of higher-order monolayers. We observed that generally when growing 3 ML CdTe NPLs, a significant contribution from 4 ML appears simultaneously and results in modified emission properties. We demonstrated that this is the result of a 3 ML/4 ML hetero-structure found within individual CdTe NPLs, resulting in both 3 and 4 ML emission accompanied by a broad trap emission. We connected these results to kinetic Monte Carlo (KMC) simulations that elucidate the differences in ripening between CdTe and CdSe NPLs. We conclude that this separation is a direct result of thermodynamic differences between CdSe and CdTe bond energies.

Result and discussion:

We followed the formation of CdTe nanoplatelets following a fast injection method reported by Pedetti *et al*.[35] (with few modifications), where to synthesize 2 ML, 3 ML, and 4 ML NPLs, elemental Te in trioctylphosphine was injected into a solution of Cd(propionate)$_2$ in

octadecene with oleic acid at 180℃, 210℃ and 215℃, respectively. Thickness and lateral size were controlled by the reaction temperature and time. In Figure 1a we describe a specific reaction procedure where Te in trioctylphosphine (TOP) is injected into the solution of Cd(propionate)$_2$ in octadecene with oleic acid at temperatures, 200℃ and the mixture is maintained at that temperature for 2 hr (discussed in detail in Method Section). To follow the formation of NPLs, an aliquot from the reaction solution is taken at different time intervals to measure the change of absorption and emission spectra with time. At early times (e.g., 10 min shown in Figure 1b) a sharp excitonic peak at 428 nm and another distinguishable peak at 387 nm are observed. The lower energy peak at 428 nm has been assigned to the heavy hole (HH) transition of 2 ML thick CdTe NPLs and the higher energy peak is the light hole (LH) transition.[7]

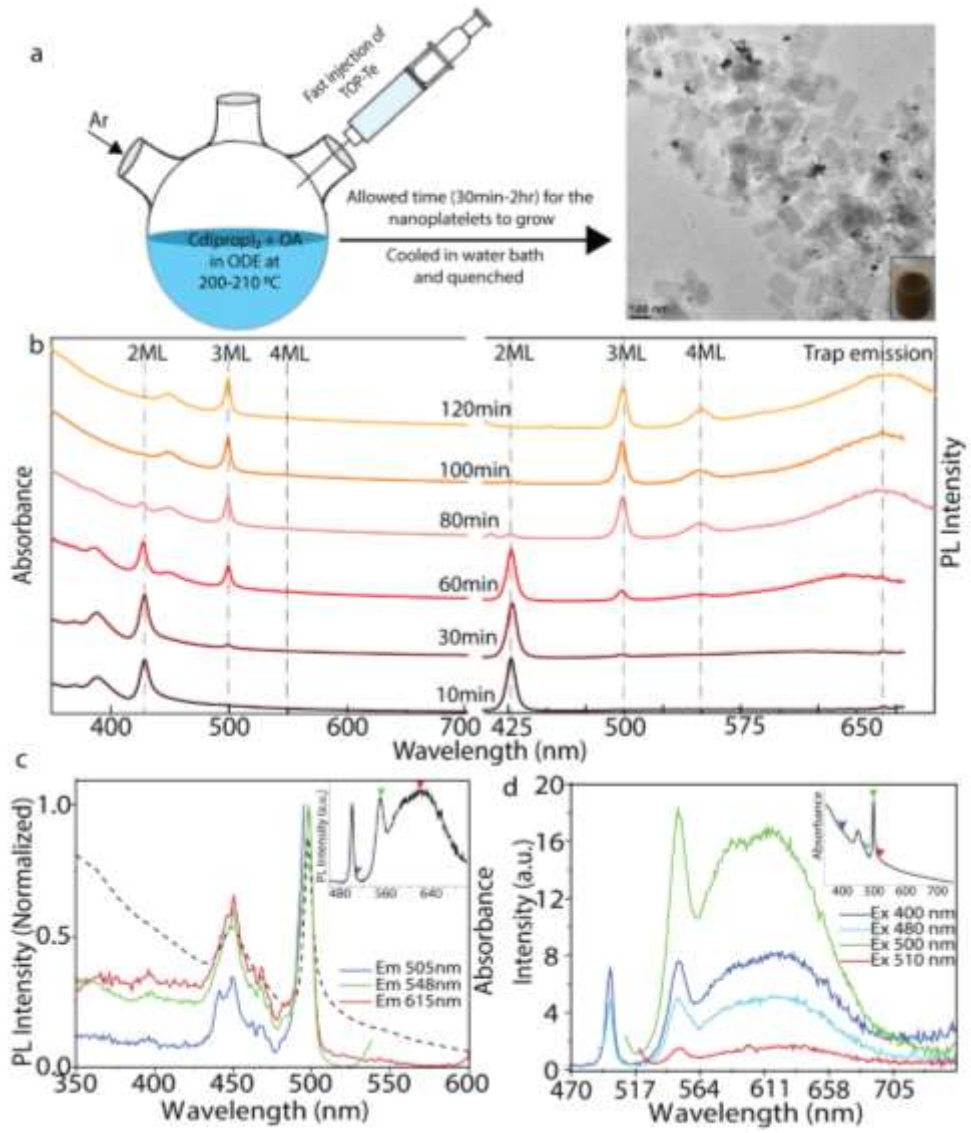

Figure 1. (a) Overview of the synthetic conditions of CdTe NPLs. The TEM image of the NPLs and an image of the colloidal dispersion are also shown, where the 3 ML NPLs are synthesized at 210 ℃ and allowed to grow for 30 min. (b) Evolution of absorption and emission spectra of CdTe NPLs during the growth period at 200 ℃. At early times, 2 ML NPLs emerge; as the time progress, the characteristic features related to 2 ML disappear while those of 3 ML appear. (c) Excitation spectra probed at different emission wavelengths and absorption spectrum (black dotted line) of 3 ML CdTe NPLs (synthesized at 210 ℃). The inset shows the emission spectrum with the emission wavelengths where the excitation spectra were recorded indicated. (d) Relative intensity variation of the emission features of the NPLs upon exciting at different wavelengths. Inset shows the absorption spectrum of the NPLs with the excitation wavelengths where the emission spectra were recorded indicated.

As time progresses, we observe the gradual disappearance of characteristic features related to 2 ML, and the appearance of new red-shifted peaks. Following precedent, we assign the sharp peak at 500 nm to the HH feature and 450 nm to the LH feature of newly formed 3 ML NPLs. The

emission spectra in Figure 1b (right panel) show the same trend. First, emission from 2 ML NPLs is observed at 429 nm, which gradually disappears, and emission at 500 nm (FWHM ~7 nm) appears, assigned to 3 ML CdTe NPLs. When the synthesis is carried out at 200℃ or lower temperatures, only 2 ML NPLs formed within the initial few minutes, and it took more than 1 hr for conversion to 3 ML. At slightly higher temperature (210℃), the reaction is faster: a mixture of 2 ML and 3 ML NPLs is always formed within the first few minutes, and it takes around 30 minutes for complete conversion to 3 ML NPLs, shown in Figure S2. Interestingly, the appearance of emission from 3 ML NPLs at 500 nm is accompanied by a sharp peak at 550 nm and a broad peak at around 615 nm (shown in the right panel of Figure 2b and Figure S2) and is observed both at 200℃ and 210℃. The broad emission feature has been reported for CdTe NPLs[34,35] and other nanocrystals[39–42] and is often attributed to emissive trap states. Although the sharp peak aligns well with 4ML emission[35,38] it could be also due to the formation of QDs, which has been observed before for HgTe NPLs[43]. However, the lack of any shift of emission over time (even at high temperature) as well as the sharp nature of the emission peak (FWHM ~ 12 nm) lead us to reject the latter possibility. Hence, this peak at 550 nm is assigned to 4 ML NPLs that appear nearly concurrently with 3 ML growth. Intriguingly, while the 4 ML NPL excitonic feature shows little contribution in absorption, it has a significant contribution to the emission spectrum (normalized plot shown in Figure S2).

In Figures 1c and 1d, we plot the emission excitation spectra and wavelength-dependent emission spectra to understand the origin of the emission features for 3 ML NPLs synthesized at 210℃. Figure 1c shows the excitation spectra for the emission at 505 nm, 548 nm and 615 nm, which match exactly with the absorption spectrum (black dotted line) of 3 ML NPLs. This suggests that the excitation of 3 ML NPL results in both 4 ML and trap emissions. To get further insight we

have recorded excitation wavelength-dependent emission spectra. Figure 1d shows that the relative emission intensity variation of all three peaks (500 nm, 550 nm and 615 nm) following excitation at the different wavelengths indicated in the inset. The emission intensity around 550 nm and 615 nm is maximized when excited at the band edge (500 nm) of the 3 ML NPLs and decreases rapidly when excited below the band-edge (> 500 nm), and no change is observed in their relative intensity. Together these results indicate that the 4ML and the broad trap emissions are correlated to the excitation of 3 ML NPLs.

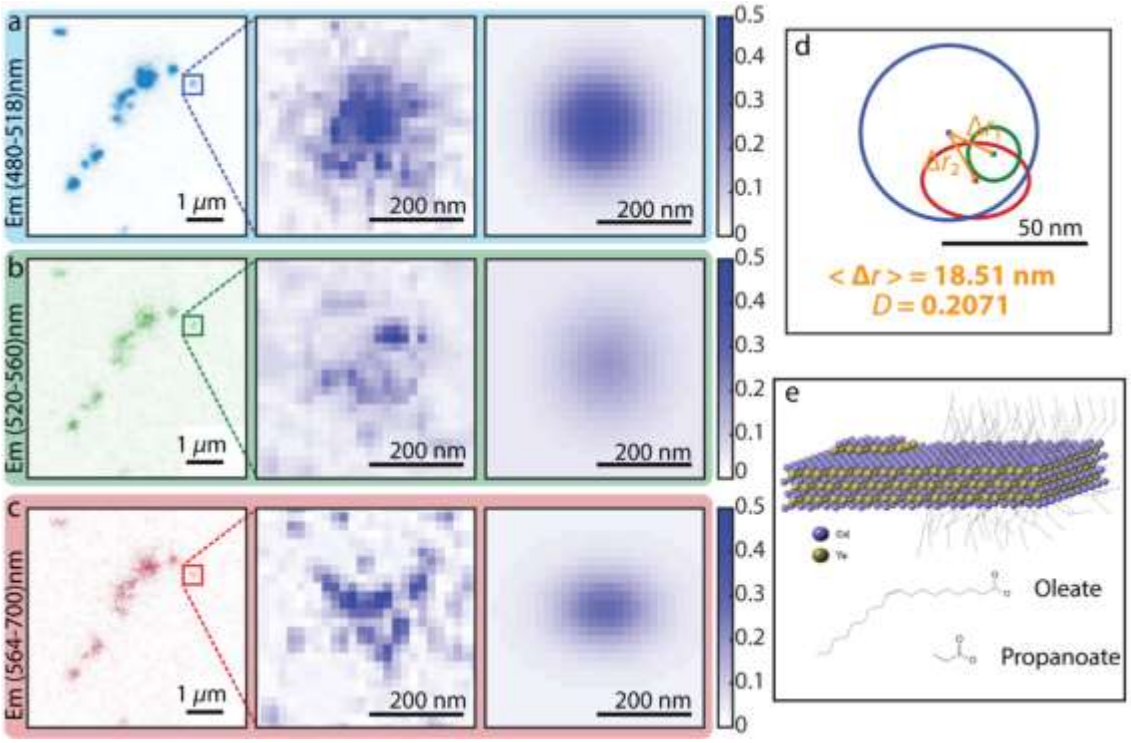

Figure 2. PL images collected at (a) 480-518 nm, (b) 520 – 560 nm, and (c) 564-700 nm. The PL from the NPL highlighted in the orange box is enlarged and then fit to a Gaussian (right panel). d) The overlap of the three Gaussians shows the spatial origin of the observed PL. (e) Schematic diagram of the hetero-confined CdTe NPL.

We next turn to understand whether all three emissions are coming from a single particle or different particles that are strongly coupled[43]. Figure S4 shows no significant change in the relative intensity of the three emission peaks, indicating that 3 ML and 4 ML NPLs are somehow physically attached. Further, we studied single-particle PL images at different emission wavelength regions. Films of NPLs were prepared from a dilute solution (~nM) of NPLs in hexane to produce well-separated single NPLs. Figure 2 shows PL imaging of the NPL film, and the three observed PL features are isolated by collecting different wavelength regions simultaneously using three detectors. The left panels of Figure 2a-2c correspond to the PL image for emission between 480-518 nm (around the 3 ML emission), 520-560 nm (around the 4 ML emission) and 564-700 nm (around the trap emission), respectively. The PL images show that there are large areas with high intensity along with smaller areas with lower intensity. The bright portions of the films are due to multiple overlapped NPLs as confirmed by atomic force microscopy (AFM; shown in Figure S5), while PL blinking of NPL in the film further supports the presence of well-dispersed single NPLs (Figure S6, video attached along with the Supporting Information). To probe single NPLs rather than multiple overlapped NPLs we chose a small, well-separated area of the film (highlighted in Figure 2a, 2b, and 2c). We observe a common overlap of all three PL features, which means 3 ML, 4 ML, and trap emission are coming from the same NPL. Further Gaussian fitting allows us to localize the center of emission for each wavelength regime with super-resolution accuracy (details in Supporting Information) and their positions are overlapped (shown in Figure 2d). However, we note a slight change in their positions and area. First, the area of NPL showing 3 ML emission is greater than that of both the 4 ML and trap emission. We calculated the distance of the center (Δr_1 and Δr_2, detail in Supporting Information) of the 4 ML and trap emission features from that of the 3 ML NPL. The average distance (Δr) for the particle shown in Figure 2d

is around 18 nm. Values calculated for more particles shown in Figure S7 vary from 15-93 nm, consistent with the dimensions of single NPLs. Emission from the 4 ML region (green circle) and trap states (red circle) appear localized near the edge in most of the NPLs. All of these observations lead us to hypothesize that an incomplete layer of 4 ML is formed near the edge of the 3 ML NPLs as shown in Figure 2e. Our hypothesis matches with the island-nucleation-limited growth model proposed by Reidinger *et al.*, which shows that the growth of an N+1 layer happens from an N layer through the formation of an island in the corner of the wide facet, which is energetically favorable and can extend from the edge to center.[8] To further quantify the localization of these features, we define a relative delocalization parameter, D, as the ratio of Δr to the average radius of the blue circle (for 3 ML emission), R_b (see Supporting Information for details). This value is around 0.20 for the particle shown in Figure 2d, where $R_b$is 0 when the Δr is 0 and $R_b$is 1 when the Δr is equal to R_b.

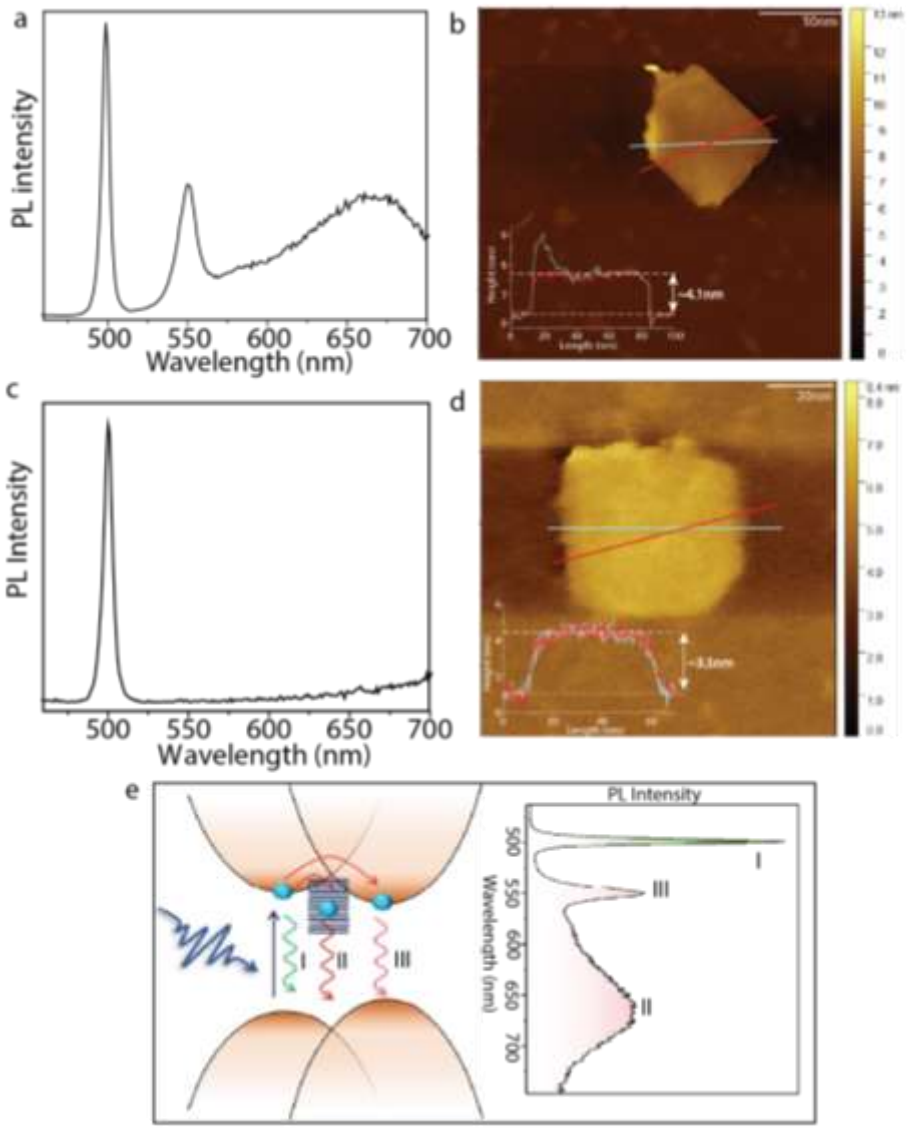

Figure 3. (a) PL spectrum and (b) AFM images of NPLs before washing. (c) PL spectrum and (d) AFM images of NPLs after washing with isopropanol. (e) Schematic diagram of the hetero-confined CdTe NPL.

We then used AFM to assess the morphology of NPL structures. The apparent height measured from AFM for a single CdTe NPL is about 4.1 nm (height profile shown in Figure 3b). The theoretically predicted thickness of 3 ML bare NPL is around 1.9 nm. In our case, the increased value could be rationalized by considering the ligand environment surrounding the NPLs.[35,44] We also observed that the height increases by approximately 1-2 nm consistently near the edges of

NPLs. This value does not exactly match a single monolayer height (~0.3 nm), but it is also much less than a separate 4ML. These areas near the edges disappear upon washing the NPLs with a polar solvent (isopropanol, details in the Methods section) as shown in Figure 3d. This washing not only smoothens the surface but also results in the disappearance of the emission peak at 550 nm and the corresponding new broad trap emission feature (Figures 3a and 3c). This is consistent with the observed PL localization and suggests a loosely bound new ML layer, removable upon gentle etching. Overall, this further supports our conclusion from the PL images that there are areas near the edges of the single 3 ML CdTe NPLs where extra monolayers are present as incipient 4 ML islands.[7] Therefore, the evidence suggests that 4 ML and trap emission do not arising from contamination by 4 ML NPLs but instead arising from hetero-confined structures, where 3 ML and 4 ML NPLs are simultaneously present.

To further test this hypothesis, we performed ultrafast transient absorption (TA) spectroscopy measurements, as shown in Figure S9. The TA spectra (Figure S9a) show a strong negative feature centered at 500 nm that arises from both the bleaching of and stimulated emission from the 3 ML exciton state.[45] The positive features on either side of the bleach correspond to the biexciton band (i.e., excited state absorption) broadened by the presence of hot carriers. A negative feature centered at the 4 ML exciton band at 550 nm is also present, becoming increasingly apparent at higher fluences (Figure S9b). The bleach recovery dynamics probed between 498 and 501 nm (Figure S9c; probe region indicated in Figure S9a) can be fit to three ultrafast components (680 ± 40 fs, 6.4 ± 0.6 ps, and 51 ± 7 ps), along with a longer component (540 ± 90 ps). Notably, the kinetics probed between 474 and 482 nm (Figure S9d; probe region indicated in Figure S9a) show the same ultrafast components (510 ± 250 fs, 4.8 ± 3.7 ps, and 70 ± 30 ps) but do not show any long-lived component. Because this excited state absorption feature is at higher energy than

the bleach, it should *only* appear when hot carriers are present; following carrier cooling, the biexciton band should lie entirely below the exciton band in energy, as discussed by Pelton *et al*.[46] Accordingly, we assign the ultrafast components to a combination of carrier cooling and thermal dissipation to the solvent and the ~0.5 ns component to radiative decay from 3ML, which likely includes exciton transfer from 3 ML to 4ML and trap states as observed before for CdSe hetero-structure with type I band alignment (shown in Figure 3e)[22] in addition to emission directly from 3 ML. The immediate appearance of a bleach feature at 550 whose dynamics match those of the 3ML bleach suggest common origin for the two features, further bolstering our hypothesis of connected states.

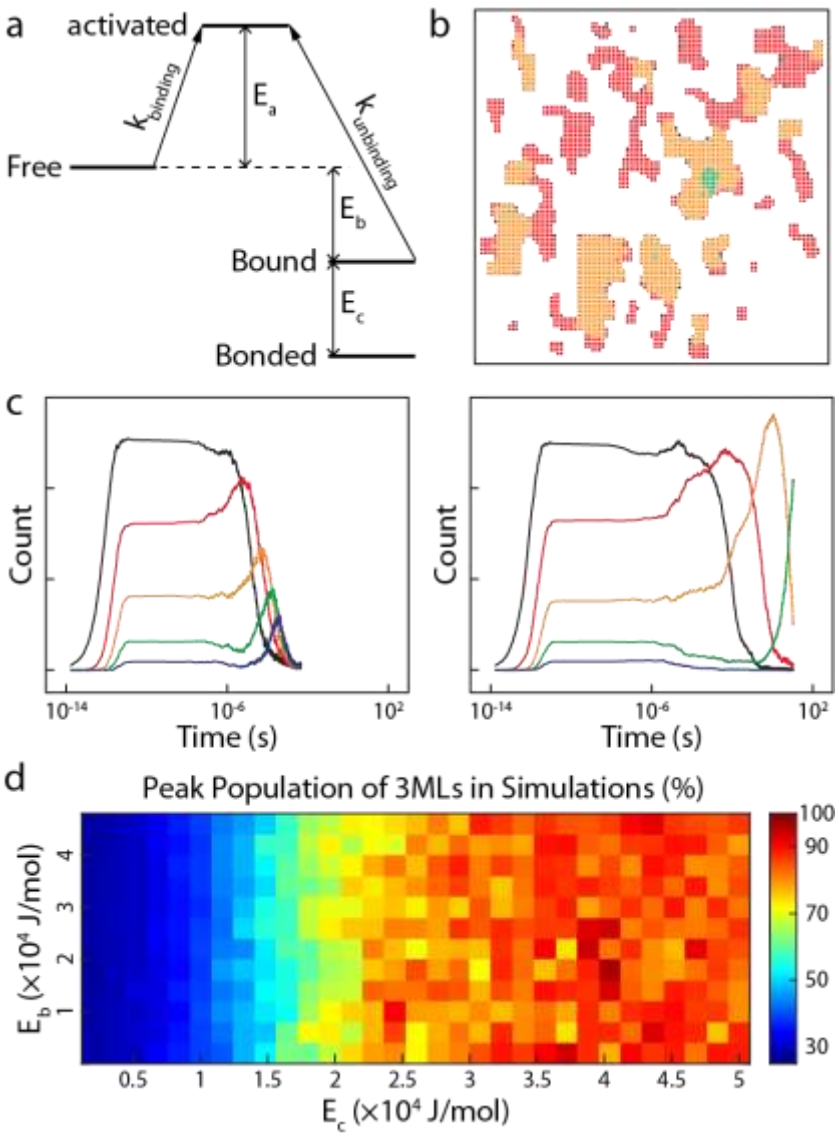

Figure 4. (a) The kinetic model applied in the kinetic Monte Carlo (KMC) simulations. Three energetic parameters are shown including the activation energy E_a, binding (nucleation) energy E_b and nearest-neighbor (NN) bond energy E_c. The energy diagram is not drawn to scale. (b) An example of the grid generated from simulations. Each small square stands for an occupied spot on the grid and the color of the square shows the number of monolayers (MLs) associated with the spot (Black: 1; Red: 2; Orange: 3; Green: 4). (c) Time evolution of populations based on two simulations. The colors of lines correspond to the number of MLs (Black: 1; Red: 2; Orange: 3; Green: 4; Blue: 5). E_a, E_b and temperature are identical for both simulations, but E_c is smaller for the simulation represented by the left graph. The time scale in both graphs is arbitrary. (See Supporting Information.) (d) A heatmap for peak population of 3 MLs based on E_b and E_c values in simulations.

The simultaneous presence of 3 ML and 4 ML appears to run contrary to the prevailing model of NPL growth by Riedinger *et al*. which strongly suggests that ripening proceeds through sequential dissolution of thinner NPLs to form thicker NPLs.[8] However, the authors of that work do note that the nucleation barrier for CdTe NPLs of different thicknesses is closer in energy than they are for CdSe or CdS. To test whether this energy difference could result in the observed hetero-confinement, we conducted a series of kinetic Monte Carlo (KMC) simulations based on a simple model of activated kinetics featuring the three most important energetic parameters: activation energy E_a, binding energy E_b and nearest-neighbor bond energy E_c, as well as temperature T (Figure 4a; also see the Methods section for details of the KMC simulations).[47] For each simulation we generate snapshots of the grid throughout the entire course of the simulation (Figure 4b). The grid can then be converted to the time evolution of different populations. We are able to produce the primary features of the ripening model from Riedinger *et al*., including the ripening of nanoplatelets (NPLs) with fewer monolayers (MLs) to those with more MLs and the apparent separation of different MLs during the growth process. (Figure 4c).[8] We then carried out a series of simulations with a wide range of values for each parameter and analyzed the resulting time evolution of populations. As a quantitative characterization of the ripening, we calculated the percentage of 3 ML population at the count peak of 3 MLs, which reflects how well separated different species are. Essentially, a higher peak population represents more "pure" NPLs in synthesis, and a lower population means more "mixed" species. As expected, changing the activation energy E_a and temperature T only led to changes in time scale but had very little influence on the species separation (see Figure S10). The results of peak populations with changing E_b and E_c are also shown, and an obvious trend of increasing peak population with increasing bond energy E_c was observed (Figure 4d). Since CdTe has lower bond energy than CdSe, the

results could explain why we were able to consistently observe the 3-4 ML heterostructure in CdTe but rarely in CdSe.[8,48]

Conclusions: Extending the superlative properties of quantum-confined NPLs to new materials and wavelengths is a critical research and technology challenge. However, despite superficial similarities between CdSe and CdTe binary semiconductors, the chemistry of CdTe does not appear to permit pure 4 ML NPLs using current methodologies. We have shown that CdTe synthesis results in a unique quantum-confined heterostructure of colocalized 3 ML and 4 ML platelets on a single NPL. Our results give a common origin for 3 ML, 4 ML, and trap emission features appearing simultaneously. We confirm this using single particle PL studies that show nearly co-localized features, further supported by AFM studies of single NPLs. Following work by Riedinger *et al*. we confirm that the low bond energy of CdTe results in weaker separation between the formation of 3 ML and 4 ML, resulting in simultaneous NPL formation. Taken together, our results thus suggest that single pot syntheses of higher ML NPL derived from CdTe following the fast injection method may suffer from incomplete separation of species and that alternative methods (e.g., colloidal atomic layer deposition) may provide a path forward for thicker NPLs.

Methods:

Materials

Cadmium oxide (Alfa Aesar, 99.95%), tellurium powder (Acros, 99.8%), oleic acid (OA) (Alfa Aesar, 99%), tri-n-octylphosphine (TOP) (Alfa Aesar, 90%), 1-octadecene (ODE) (Alfa Aesar, 90%), isopropanol, hexanes (Fisher, 98.5%) and propionic acid (Fisher) were used without further purification.

Synthesis of Precursors

Cadmium propionate ($Cd(prop)_2$): 1.036 g of CdO powder was mixed with 10 mL propionic acid under Ar flow for 1 hour. The flask was then heated at 140 ˚C after opening to atmosphere in order to reduce the volume by half. The white solution was precipitated with acetone and centrifuged. The supernatant was discarded, and the solid was dried and stored in a vacuum desiccator.

TOP-Te (1 M): In a small flask, 0.254 g of Te powder and 2 mL of tri-*n*-octylphosphine were degassed under vacuum at room temperature. Then, under Ar flow, the solution was stirred at 275 ˚C until the dissolution was complete, and the solution turned yellow. The solution was cooled and stored under Argon.

Cadmium oleate (Cd-oleate): 0.96 g of CdO (7.5 mmol) and 15 mL of oleic acid were charged into a 25 mL round bottom flask. The mixture was heated at 200 ℃ for 1 hr under Ar flow. Once the solution turned colorless, the mixture was brought to 60 ℃ and degassed for 1 hr. After this, it was stored at room temperature and subsequently used in the reactions described below.

Synthesis of CdTe NPLs: In a three-neck 50 mL flask, 130 mg of $Cd(prop)_2$ (0.5 mmol), 80 µL of oleic acid (0.25 mmol) and 10 mL of ODE was magnetically stirred and degassed under vacuum at 80 ℃ for 2 h. The mixture was then put under Ar and heated to 200-210 ℃. When the desired temperature was reached, 100 µL of a solution of 1 M TOP-Te diluted in 0.5 mL of ODE was swiftly added. The reaction was maintained at the same temperature for the NPLs to grow with time. An aliquot from the reaction solution was taken out at different time intervals. It was centrifuged at 7000 rpm and dispersed in hexanes and characterized by the absorption and PL spectrum. For the remaining measurements, the reaction was performed at 210 ℃. After the TOP-

Te injection, the reaction was allowed to continue for 30 mins after which the heating mantle was removed. When the flask was cooled down to about 120 °C, 1 mL $Cd(oleate)_2$, separately heated to 100 °C was injected and the reaction was quenched. The solution was then divided into two halves. Only hexane (10 mL) was added to one portion, while hexane (10 mL) and isopropanol (5 mL) were added to the other portion. Both were centrifuged at 7000 rpm for 10 mins. The supernatant was discarded and the solid precipitate was re-dispersed in hexane. We assumed that the reaction goes to completion and yield is 100%. Following centrifugation and resuspension in 20ML hexanes the [Te] will be 5mM in the original CdTe NPLs.

KMC simulation algorithm: In a typical simulation, we start with a number of free 'monomers' and an empty grid. Monomers here could describe small clusters, unit cells, or other reactive precursors. We then drive the system forward by the events of free monomers binding to the grid and bound monomers unbinding from the grid. The events are characterized by the rates of binding and unbinding:

$$k_{\text{binding}} = P_b \exp\left(-\frac{E_a}{RT}\right), k_{\text{unbinding}} = P_u \exp\left(-\frac{E_a+E_b}{RT}\right) \quad (1)$$

where E_a is the activation energy for binding, E_b is the binding energy (i.e., the energy difference between free and bound monomers), and P_b, P_u are the pre-factors for the Arrhenius rate equations.

In addition to the interactions between monomers and the grid, we also consider bond-forming between bound monomers in real synthesis. For simplicity, we assume that every

monomer will form bonds with its nearest neighbors (NNs), thus lowering its energy linearly with the number of NNs and further decreasing the unbinding rate of bonded bound monomers:

$$k_{\text{unbinding,bonded}} = P_u \exp(-\frac{E_a+E_b+E_c}{RT}) \quad (2)$$

For all the rate equations, the pre-factors can be estimated based on the diffusion-limited reactions:

$$P_b = \frac{8Nk_BT}{3\eta}, P_u = \frac{k_BT}{4\pi\eta R_M^3} \quad (3)$$

where η is the dynamic viscosity of the solvent, N is the number density of free monomers and R_M is the hydrodynamic radius of monomers.[49] As mentioned, the exact composition or structure of monomers is uncertain, resulting in ambiguity in the value of R_M. Thus, the actual time drawn from simulations are simply representative, but the *relative* timescales can be used for comparison.

With the calculated rate equations, we then generate a rate matrix with each element of the matrix corresponding to the sum of rate for each spot on the grid, which includes rates for all possible events taking place at the spot (i.e., binding and unbinding):

$$k_{i,j} = k_{\text{binding}\rightarrow(i,j)} + k_{\text{unbinding}\leftarrow(i,j)} \quad (4)$$

where $k_{i,j}$ is the rate matrix element, $k_{\text{binding}\rightarrow(i,j)}$ is the rate of free monomers binding to the spot (i,j) on the grid, and $k_{\text{unbinding}\leftarrow(i,j)}$ is the rate of monomers bound at the spot (i,j) desorbing from the grid. The pathway is then selected using the BKL algorithm[50] which takes advantage of

partial sum of rates by drawing two random numbers, one for determining at which spot an event happens, and the other for determining what type the event is.

After the pathway selection, the clock is advanced by drawing a third random number:

$$t = -\frac{\ln(\text{rand})}{\sum_{i,j} k_{i,j}} \quad (5)$$

At each step, the statistics of the number of spots with different number of monolayers (MLs) are calculated along with the clock time.

Corresponding Author

***E-mail: jcaram@chem.ucla.edu.**

Author Contributions

#T.A. and X.T. contributed equally to this work. T.A. synthesized and characterized all materials along with help from S.M.T. and E.C. All the KMC was done by X.T. The 2D fitting of the photoluminescence imaging was done by B.Y.L. J.W. assisted with recording AFM images. S.M.T.† and D.H. recorded and analyzed the TA data.

Funding Sources

This work was supported by NSF Career Grant CHE-194572, and the California Interfacial Science Institute (UC- MRPI CISI).

Acknowledgements

We thank the Materials Characterization Laboratory at UCLA for instrumentation. We acknowledge the use of instruments at the Electron Imaging Center for NanoMachines and Advanced light Microscopy and Spectroscopy Lab in CNSI at UCLA.

Supporting Information

The following files are available free of charge.

- Additional experimental details, details of 2D fitting of PL images, additional characterization including absorption and photoluminescence, photoluminescence lifetimes, AFM images, PL images and 2D fitting, PL blinking trace, TA spectra and kinetics, Ea and T tuning.
- Single particle blinking video for CdTe NPLs

References:

(1) Peng, X.; Manna, L.; Yang, W.; Wickham, J.; Scher, E.; Kadavanich, A.; Alivisatos, A. P. Shape Control of CdSe Nanocrystals. *Nature* **2000**, *404* (6773). https://doi.org/10.1038/35003535.

(2) Murray, C. B.; Norris, D. J.; Bawendi, M. G. Synthesis and Characterization of Nearly Monodisperse CdE (E = S, Se, Te) Semiconductor Nanocrystallites. *J Am Chem Soc* **1993**, *115* (19). https://doi.org/10.1021/ja00072a025.

(3) Hu, Z.; O'Neill, R.; Lesyuk, R.; Klinke, C. Colloidal Two-Dimensional Metal Chalcogenides: Realization and Application of the Structural Anisotropy. *Acc Chem Res* **2021**, *54* (20). https://doi.org/10.1021/acs.accounts.1c00209.

(4) Sharma, M.; Delikanli, S.; Demir, H. V. Two-Dimensional CdSe-Based Nanoplatelets: Their Heterostructures, Doping, Photophysical Properties, and Applications. *Proceedings of the IEEE* **2020**, *108* (5). https://doi.org/10.1109/JPROC.2019.2944277.

(5) Zhang, J.; Sun, Y.; Ye, S.; Song, J.; Qu, J. Heterostructures in Two-Dimensional CdSe Nanoplatelets: Synthesis, Optical Properties, and Applications. *Chemistry of Materials*. 2020. https://doi.org/10.1021/acs.chemmater.0c02593.

(6) Tenney, S. M.; Tan, L. A.; Sonnleitner, M. L.; Sica, A. V.; Shin, A. J.; Ronquillo, R.; Ahmed, T.; Atallah, T. L.; Caram, J. R. Mesoscale Quantum-Confined Semiconductor Nanoplatelets through Seeded Growth. *Chemistry of Materials* **2022**, *34* (13), 6048–6056. https://doi.org/10.1021/acs.chemmater.2c01144.

(7) Naeem, A.; Masia, F.; Christodoulou, S.; Moreels, I.; Borri, P.; Langbein, W. Giant Exciton Oscillator Strength and Radiatively Limited Dephasing in Two-Dimensional Platelets. *Phys Rev B Condens Matter Mater Phys* **2015**, *91* (12). https://doi.org/10.1103/PhysRevB.91.121302.

(8) Riedinger, A.; Ott, F. D.; Mule, A.; Mazzotti, S.; Knüsel, P. N.; Kress, S. J. P.; Prins, F.; Erwin, S. C.; Norris, D. J. An Intrinsic Growth Instability in Isotropic Materials Leads to Quasi-Two-Dimensional Nanoplatelets. *Nat Mater* **2017**, *16* (7), 743–748. https://doi.org/10.1038/nmat4889.

(9) Rowland, C. E.; Fedin, I.; Zhang, H.; Gray, S. K.; Govorov, A. O.; Talapin, D. V.; Schaller, R. D. Picosecond Energy Transfer and Multiexciton Transfer Outpaces Auger Recombination in Binary CdSe Nanoplatelet Solids. *Nat Mater* **2015**, *14* (5). https://doi.org/10.1038/nmat4231.

(10) Yeltik, A.; Delikanli, S.; Olutas, M.; Kelestemur, Y.; Guzelturk, B.; Demir, H. V. Experimental Determination of the Absorption Cross-Section and Molar Extinction Coefficient of Colloidal CdSe Nanoplatelets. *Journal of Physical Chemistry C* **2015**, *119* (47). https://doi.org/10.1021/acs.jpcc.5b09275.

(11) Yu, J.; Chen, R. Optical Properties and Applications of Two-Dimensional CdSe Nanoplatelets. *InfoMat*. Blackwell Publishing Ltd September 1, 2020, pp 905–927. https://doi.org/10.1002/inf2.12106.

(12) Lhuillier, E.; Pedetti, S.; Ithurria, S.; Heuclin, H.; Nadal, B.; Robin, A.; Patriarche, G.; Lequeux, N.; Dubertret, B. Electrolyte-Gated Field Effect Transistor to Probe the Surface Defects and Morphology in Films of Thick CdSe Colloidal Nanoplatelets. *ACS Nano* **2014**, *8* (4). https://doi.org/10.1021/nn500538n.

(13) She, C.; Fedin, I.; Dolzhnikov, D. S.; Demortière, A.; Schaller, R. D.; Pelton, M.; Talapin, D. V. Low-Threshold Stimulated Emission Using Colloidal Quantum Wells. *Nano Lett* **2014**, *14* (5). https://doi.org/10.1021/nl500775p.

(14) She, C.; Fedin, I.; Dolzhnikov, D. S.; Dahlberg, P. D.; Engel, G. S.; Schaller, R. D.; Talapin, D. V. Red, Yellow, Green, and Blue Amplified Spontaneous Emission and Lasing Using Colloidal CdSe Nanoplatelets. *ACS Nano* **2015**, *9* (10). https://doi.org/10.1021/acsnano.5b02509.

(15) Guzelturk, B.; Kelestemur, Y.; Olutas, M.; Delikanli, S.; Demir, H. V. Amplified Spontaneous Emission and Lasing in Colloidal Nanoplatelets. *ACS Nano* **2014**, *8* (7). https://doi.org/10.1021/nn5022296.

(16) Ithurria, S.; Bousquet, G.; Dubertret, B. Continuous Transition from 3D to 1D Confinement Observed during the Formation of CdSe Nanoplatelets. *J Am Chem Soc* **2011**, *133* (9). https://doi.org/10.1021/ja110046d.

(17) Ott, F. D.; Riedinger, A.; Ochsenbein, D. R.; Knüsel, P. N.; Erwin, S. C.; Mazzotti, M.; Norris, D. J. Ripening of Semiconductor Nanoplatelets. *Nano Lett* **2017**, *17* (11). https://doi.org/10.1021/acs.nanolett.7b03191.

(18) Khan, A. H.; Bertrand, G. H. V.; Teitelboim, A.; Sekhar M, C.; Polovitsyn, A.; Brescia, R.; Planelles, J.; Climente, J. I.; Oron, D.; Moreels, I. CdSe/CdS/CdTe Core/Barrier/Crown Nanoplatelets: Synthesis, Optoelectronic Properties, and Multiphoton Fluorescence Upconversion. *ACS Nano* **2020**, *14* (4). https://doi.org/10.1021/acsnano.9b09147.

(19) Pedetti, S.; Ithurria, S.; Heuclin, H.; Patriarche, G.; Dubertret, B. Type-II CdSe/CdTe Core/Crown Semiconductor Nanoplatelets. *J Am Chem Soc* **2014**, *136* (46). https://doi.org/10.1021/ja509307m.

(20) Mahler, B.; Nadal, B.; Bouet, C.; Patriarche, G.; Dubertret, B. Core/Shell Colloidal Semiconductor Nanoplatelets. *J Am Chem Soc* **2012**, *134* (45). https://doi.org/10.1021/ja307944d.

(21) Diroll, B. T.; Guzelturk, B.; Po, H.; Dabard, C.; Fu, N.; Makke, L.; Lhuillier, E.; Ithurria, S. 2D II-VI Semiconductor Nanoplatelets: From Material Synthesis to Optoelectronic Integration. *Chemical Reviews*. 2023. https://doi.org/10.1021/acs.chemrev.2c00436.

(22) Moghaddam, N.; Dabard, C.; Dufour, M.; Po, H.; Xu, X.; Pons, T.; Lhuillier, E.; Ithurria, S. Surface Modification of CdE (E: S, Se, and Te) Nanoplatelets to Reach Thicker Nanoplatelets and Homostructures with Confinement-Induced Intraparticle Type I Energy Level Alignment. *J Am Chem Soc* **2021**, *143* (4). https://doi.org/10.1021/jacs.0c10336.

(23) Dufour, M.; Qu, J.; Greboval, C.; Méthivier, C.; Lhuillier, E.; Ithurria, S. Halide Ligands to Release Strain in Cadmium Chalcogenide Nanoplatelets and Achieve High Brightness. *ACS Nano* **2019**, *13* (5). https://doi.org/10.1021/acsnano.8b09794.

(24) Pan, J.; Qian, Y. Synthesis of Cadmium Chalcogenide Nanotubes at Room Temperature. *Mater Lett* **2012**, *85*. https://doi.org/10.1016/j.matlet.2012.07.012.

(25) Sun, J.; Buhro, W. E.; Wang, L. W.; Schrier, J. Electronic Structure and Spectroscopy of Cadmium Telluride Quantum Wires. *Nano Lett* **2008**, *8* (9). https://doi.org/10.1021/nl801737m.

(26) Tang, Z.; Zhang, Z.; Wang, Y.; Glotzer, S. C.; Kotov, N. A. Self-Assembly of CdTe Nanocrystals into Free-Floating Sheets. *Science (1979)* **2006**, *314* (5797). https://doi.org/10.1126/science.1128045.

(27) Xie, X.; Kwok, S. Y.; Lu, Z.; Liu, Y.; Cao, Y.; Luo, L.; Zapien, J. A.; Bello, I.; Lee, C. S.; Lee, S. T.; Zhang, W. Visible-NIR Photodetectors Based on CdTe Nanoribbons. *Nanoscale* **2012**, *4* (9). https://doi.org/10.1039/c2nr30277b.

(28) Sun, H.; Buhro, W. E. Contrasting Ligand-Exchange Behavior of Wurtzite and Zinc-Blende Cadmium Telluride Nanoplatelets. *Chemistry of Materials* **2021**, *33* (5). https://doi.org/10.1021/acs.chemmater.0c04247.

(29) Sun, H.; Wang, F.; Buhro, W. E. Tellurium Precursor for Nanocrystal Synthesis: Tris(Dimethylamino)Phosphine Telluride. *ACS Nano* **2018**, *12* (12). https://doi.org/10.1021/acsnano.8b06468.

(30) Wang, F.; Javaid, S.; Chen, W.; Wang, A.; Buntine, M. A.; Jia, G. Synthesis of Atomically Thin CdTe Nanoplatelets by Using Polytelluride Tellurium Precursors. *Aust J Chem* **2021**, *74* (3). https://doi.org/10.1071/CH20174.

(31) Yu, W. W.; Wang, Y. A.; Peng, X. Formation and Stability of Size-, Shape-, and Structure-Controlled CdTe Nanocrystals: Ligand Effects on Monomers and Nanocrystals. *Chemistry of Materials* **2003**, *15* (22). https://doi.org/10.1021/cm034729t.

(32) Karl, N. Landolt-Börnstein. Numerical Data and Functional Relationships in Science and Technology (New Series) Group III: Crystal and Solid State Physics. Vol. 17. *Crystal Research and Technology* **1988**, *17*.

(33) Gur, I.; Fromer, N. A.; Chen, C. P.; Kanaras, A. G.; Alivisatos, A. P. Hybrid Solar Cells with Prescribed Nanoscale Morphologies Based on Hyperbranched Semiconductor Nanocrystals. *Nano Lett* **2007**, *7* (2). https://doi.org/10.1021/nl062660t.

(34) Ithurria, S.; Tessier, M. D.; Mahler, B.; Lobo, R. P. S. M.; Dubertret, B.; Efros, A. L. Colloidal Nanoplatelets with Two-Dimensional Electronic Structure. *Nat Mater* **2011**, *10* (12), 936–941. https://doi.org/10.1038/nmat3145.

(35) Pedetti, S.; Nadal, B.; Lhuillier, E.; Mahler, B.; Bouet, C.; Abécassis, B.; Xu, X.; Dubertret, B. Optimized Synthesis of CdTe Nanoplatelets and Photoresponse of CdTe Nanoplatelets Films. *Chemistry of Materials* **2013**, *25* (12), 2455–2462. https://doi.org/10.1021/cm4006844.

(36) Chu, A.; Livache, C.; Ithurria, S.; Lhuillier, E. Electronic Structure Robustness and Design Rules for 2D Colloidal Heterostructures. *J Appl Phys* **2018**, *123* (3). https://doi.org/10.1063/1.5003289.

(37) Anand, A.; Zaffalon, M. L.; Cova, F.; Pinchetti, V.; Khan, A. H.; Carulli, F.; Brescia, R.; Meinardi, F.; Moreels, I.; Brovelli, S. Optical and Scintillation Properties of Record-Efficiency CdTe Nanoplatelets toward Radiation Detection Applications. *Nano Lett* **2022**, *22* (22), 8900–8907. https://doi.org/10.1021/acs.nanolett.2c02975.

(38) AL-Shnani, F.; Mutyala, C. S.; Rodà, C.; Moreels, I. Fluorescence Quantum Efficiency Enhancement in Size-Controlled 3.5 Monolayer Cadmium Telluride Nanoplatelets. *Chemistry of Materials* **2023**, *35* (16). https://doi.org/10.1021/acs.chemmater.3c00690.

(39) Sui, X.; Gao, X.; Wu, X.; Li, C.; Yang, X.; Du, W.; Ding, Z.; Jin, S.; Wu, K.; Sum, T. C.; Gao, P.; Liu, J.; Wei, X.; Zhang, J.; Zhang, Q.; Tang, Z.; Liu, X. Zone-Folded Longitudinal Acoustic Phonons Driving Self-Trapped State Emission in Colloidal CdSe Nanoplatelet Superlattices. *Nano Lett* **2021**, *21* (10). https://doi.org/10.1021/acs.nanolett.0c04169.

(40) Hinterding, S. O. M.; Salzmann, B. B. V.; Vonk, S. J. W.; Vanmaekelbergh, D.; Weckhuysen, B. M.; Hutter, E. M.; Rabouw, F. T. Single Trap States in Single CdSe Nanoplatelets. *ACS Nano* **2021**, *15* (4). https://doi.org/10.1021/acsnano.1c00481.

(41) Van Der Stam, W.; De Graaf, M.; Gudjonsdottir, S.; Geuchies, J. J.; Dijkema, J. J.; Kirkwood, N.; Evers, W. H.; Longo, A.; Houtepen, A. J. Tuning and Probing the Distribution of Cu+ and Cu2+ Trap States Responsible for Broad-Band Photoluminescence in CuInS2 Nanocrystals. *ACS Nano* **2018**, *12* (11). https://doi.org/10.1021/acsnano.8b05843.

(42) Kushwaha, M.; Srivastava, A. P.; Singh, M. K. Balanced Emission from Band-Edge and Trap States of Ultra Stable CdSe Nanocrystals Synthesized by Aqueous Route. *Mater Lett* **2013**, *109*. https://doi.org/10.1016/j.matlet.2013.07.028.

(43) Tenney, S. M.; Tan, L. A.; Tan, X.; Sonnleitner, M. L.; Coffey, B.; Williams, J. A.; Ronquillo, R.; Atallah, T. L.; Ahmed, T.; Caram, J. R. Efficient 2D to 0D Energy Transfer in HgTe Nanoplatelet-

Quantum Dot Heterostructures through High-Speed Exciton Diffusion. *Journal of Physical Chemistry Letters* **2023**, *14* (42). https://doi.org/10.1021/acs.jpclett.3c02168.

(44) Peric, N.; Lambert, Y.; Singh, S.; Khan, A. H.; Vergel, N. A. F.; Deresmes, D.; Berthe, M.; Hens, Z.; Moreels, I.; Delerue, C.; Grandidier, B.; Biadala, L. Van Hove Singularities and Trap States in Two-Dimensional CdSe Nanoplatelets. *Nano Lett* **2021**, *21* (4). https://doi.org/10.1021/acs.nanolett.0c04509.

(45) Morgan, D. P.; Maddux, C. J. A.; Kelley, D. F. Transient Absorption Spectroscopy of CdSe Nanoplatelets. *Journal of Physical Chemistry C* **2018**, *122* (41). https://doi.org/10.1021/acs.jpcc.8b07733.

(46) Pelton, M.; Ithurria, S.; Schaller, R. D.; Dolzhnikov, D. S.; Talapin, D. V. Carrier Cooling in Colloidal Quantum Wells. *Nano Lett* **2012**, *12* (12). https://doi.org/10.1021/nl302986y.

(47) Voter, A. F. INTRODUCTION TO THE KINETIC MONTE CARLO METHOD. In *Radiation Effects in Solids*; 2007. https://doi.org/10.1007/978-1-4020-5295-8_1.

(48) Xiang, X.; Wang, L.; Zhang, J.; Cheng, B.; Yu, J.; Macyk, W. Cadmium Chalcogenide (CdS, CdSe, CdTe) Quantum Dots for Solar-to-Fuel Conversion. *Adv Photonics Res* **2022**, *3* (11). https://doi.org/10.1002/adpr.202200065.

(49) Shoup, D.; Szabo, A. Role of Diffusion in Ligand Binding to Macromolecules and Cell-Bound Receptors. *Biophys J* **1982**, *40* (1). https://doi.org/10.1016/S0006-3495(82)84455-X.

(50) Bortz, A. B.; Kalos, M. H.; Lebowitz, J. L. A New Algorithm for Monte Carlo Simulation of Ising Spin Systems. *J Comput Phys* **1975**, *17* (1). https://doi.org/10.1016/0021-9991(75)90060-1.